Then the equation $[A]\{\partial \Phi_C/\partial\mu_a\} = \{\partial S/\partial\mu_a\}\ [\partial A/\partial\mu_a]\{\Phi_C\}$ enables one to compute $\partial\Phi_C/\partial\mu_a$ (and a similar forward problem enables the computation of $\partial\Phi_C/\partial D$).[108] This approach is optimal with finite elements; because the numerical formulation lends itself easily to taking the derivative of [A]. Φ_C, [A] and $[A]^{-1}$ are updated on each iteration. The *adjoint* approach solves the forward problem $[A]\{\Phi_C\} = \{S\}$ to determine Φ_C, and an adjoint problem $[A^*]\{G\} = \{S'\}$ to determine Green's function $G(\mathbf{r}_d,\mathbf{r})$ due to a unit source at the detector position.[1,102–105,107,119,120] G and Φ_c then fix the elements of [J] according to Equation 21.15. Both Φ_c and G are updated at each iteration. The impact of the two different approaches on convergence and accuracy is not well understood. However, from the computational perspective, for each iteration the direct approach requires 3NS solves per iteration, while the adjoint Born or Rytov approach requires *NS* plus *ND* solves per iteration.

The inverse problem, $[J]\ \{\Delta\mu_a, \Delta D\}^T = \{\Phi_M - \Phi_C\}$, which is also a matrix equation, is significantly more costly than these other subproblems because the Jacobian is a full nonsquare matrix $\{NM \times 2NV\}$. However, the inverse problem only needs to be solved once per iteration cycle. The Jacobian is ill-conditioned and is thus singular or close to singular, which makes it difficult to invert directly. Generally, the approach to address these issues is twofold. First, the matrix is made square by multiplying the inverse problem by the transpose of the Jacobian, i.e.,

$$[J]^T[J]\{\Delta\mu_a,\Delta D\}^T = [J]^T\{\Phi_M - \Phi_C\}. \tag{21.16}$$

Unfortunately, by squaring the Jacobian the equation becomes even more ill conditioned. This problem is solved by regularization[121,122] so that the equation becomes

$$\left([J]^T[J] + \lambda[C]^T[C]\right)\{\Delta\mu_a,\Delta D\}^T = [J]^T\{\Phi_M - \Phi_C\}. \tag{21.17}$$

Here λ is called the regularization parameter and [C] is the regularizing operator, which is sometimes taken to be the identity matrix. The regularization parameter generally is related to the measurement signal-to-noise. It is a theoretical "knob" that can be adjusted and it will affect image quality by introducing a trade-off between spatial resolution and contrast.[122,123] Nevertheless, its use converts the inverse problem into a readily solvable problem. $\{\Delta\mu_a, \Delta D\}^T$ can now be determined using Equation 21.17 and any number of mathematical techniques that solve systems of linear equations. A particularly useful and common solution scheme is the conjugate gradient method.

A qualitatively different scheme due to Arridge involves the implicit determination of the Jacobian. Briefly, this technique utilizes the Born or Rytov approximation for the inverse problem, and has at least two known solution methods: gradient-based iterative technique and ART (algebraic reconstruction technique). The Jacobian is not calculated; instead an objective function (e.g., a chi-square function) is defined whose gradient, for example, can be used to derive subsequent search directions (see the original papers, References 114 and 118, for details.) Note that the implicit formulation is particularly attractive for experimental systems that rely on many detectors rather than many sources.

21.2.5.4 Challenges for Implementation

The main barrier for full three-dimensional reconstruction is the significant memory and processing time it requires. There are three costly steps of the algorithms: (1) solving the forward problem for each source position, (2) determining the Jacobian, and (3) solving the inverse problem. The forward problem requires the solution of a matrix equation banded in finite difference or sparse in finite elements. The solvers in three-dimensional reconstruction are necessarily iterative because direct solvers require very large storage space for full matrices. Subsequently, multiple source positions demand multiple forward solves. Determination of the Jacobian requires additional matrix equation solutions. For explicit determination, the Green's function for each detector position is needed or the vectors $\partial\Phi_C/\partial\mu_a$ and $\partial\Phi_C/\partial D$ are needed.

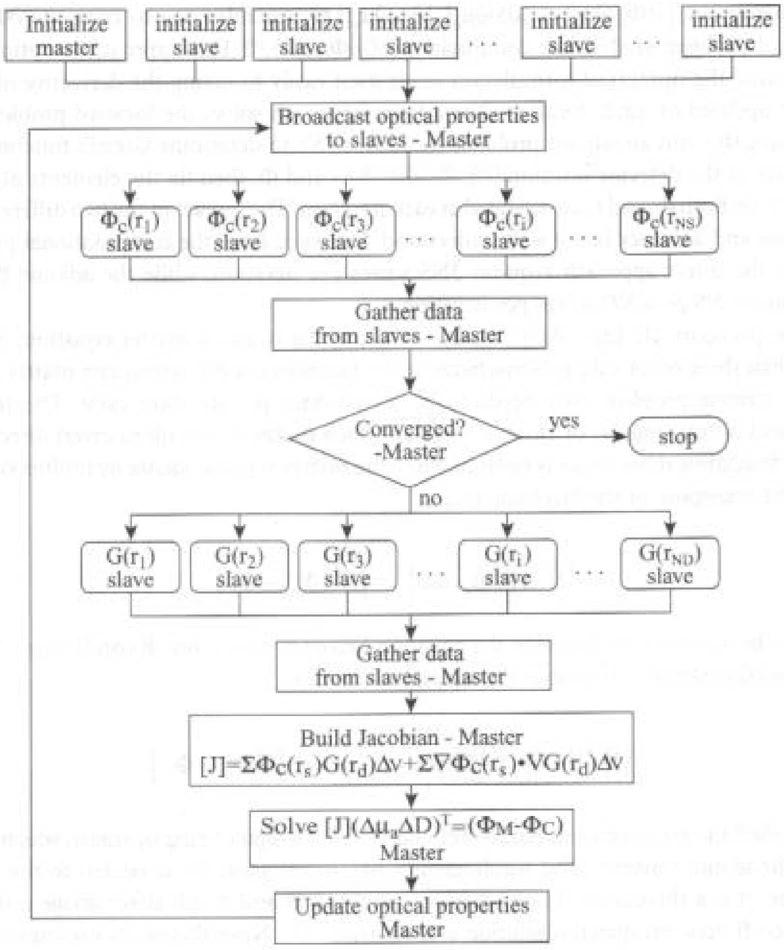

FIGURE 21.4 Schematic of the University of Pennsylvania algorithm for image reconstruction using parallel computing. In the first step each node has its own set of arrays and variables that are initialized. The master must initialize the Jacobian array, the forward solution vector array, and the Green's function vector array. In the second step the master sends out the optical properties, which (in the first iteration) are just the background values. In the third step, the slaves calculate the solutions to the forward problem; *NS* slaves are used in this step. The solution vectors are then returned to the master and at this point the master checks for convergence. If convergence has not been achieved then the slaves calculate the solutions to the Green's function; *ND* slaves are used in this step. The solution vectors are returned to the master and the Jacobian is determined. Next the master solves the inverse problem, in this case by using a spatially variant regularized conjugate gradient optimization method. Finally, the optical properties are updated on the master and the algorithm repeats until convergence has been achieved.

Consider a system with one frequency — *NS* sources and *ND* detectors; assume further that all the detectors are used for each source. The number of measurements is $NM = NS \times ND$. For each iteration we require *NS* forward solves and, depending on the Jacobian determination, either *ND* Green's function or 2*NS* solves for the vectors $\partial\Phi_C/\partial\mu_a$ and $\partial\Phi_C/\partial D$ (implicit would require *NS* solves). The final costly step of the algorithm is the solution of the inverse problem. However, the inverse problem only needs to be solved once per iteration cycle. For many practical problems the calculations take a long time, and limited memory is available to store the Jacobian explicitly. An important solution to this large-scale computational problem is parallel computing — the execution of many computations at one time using many processors. It has been used successfully in areas of medical imaging, such as positron emission tomography (PET),[124–128] single photon emission computed tomography (SPECT),[129,130] computed tomography (CT),[131–133] electrical impedance tomography (EIT),[134] and optical sectioning microscopy

(OSM).[135] It is just beginning to catch on in the diffuse optical tomography (DOT) community.[136,137] In Figure 21.4, we illustrate how the problem is parallelized at the University of Pennsylvania.

21.2.6 Diffusion of Light Correlations: Blood Flow

Thus far our discussion has centered around the determination of tissue absorption and scattering properties. Among other things, these measurements provide access to concentrations of oxygenated and deoxygenated hemoglobin. Even more information, however, is impressed upon these diffusing light fields. Speckle fluctuations of the scattered light are sensitive to the motions of scatterers such as red blood cells.

The means for using light fluctuations and light frequency shifts to study motions have appeared with numerous names over the years.[138–158] In most of these experiments the quantity of interest is the electric field temporal autocorrelation function $G_1(\mathbf{r},\tau) = \langle E(\mathbf{r},t)\, E^*(\mathbf{r}, t + \tau)\rangle$ or its Fourier transform. Here the angle brackets $\langle\,\rangle$ denote ensemble averages or averages over time for most systems of practical interest. τ is called the correlation time. The field correlation function is explicitly related to the motions of scatterers within the samples that we study.

The study of these motions in deep tissues is possible because the electric field temporal autocorrelation function for light traveling in highly scattering media also obeys a diffusion equation.[152] In steady-state (i.e., $\omega = 0$) and in homogeneous media, this correlation diffusion equation is quite simple:

$$\left(D\nabla^2 - v\mu_a - \alpha k_o^2 \mu_s' \left\langle \Delta \mathbf{r}^2(\tau)\right\rangle / 3\right) G_1(\mathbf{r},\tau) = -vS(\mathbf{r})\,. \tag{21.18}$$

Here k_o is the wavevector of the photons in the medium and $\langle \Delta\mathbf{r}^2(\tau)\rangle$ is the mean-square displacement in time τ of the scattering particles (e.g., blood cells); it can have different forms depending on the nature of the particle motion and can also vary with position. $S(\mathbf{r})$ is the source light distribution, and α represents the fraction of photon scattering events in the tissue that occur from moving cells or particles.

Notice that, for $\tau \to 0$, $\langle \Delta\mathbf{r}^2(\tau)\rangle \to 0$, and Equation 21.18 reduces to the steady-state diffusion equation for diffuse photon fluence rate (i.e., Equation 21.8 with $\omega = 0$). Notice also that the homogenous version of Equation 21.18 can be recast as a Helmholtz-like equation for the temporal field autocorrelation function, $G_1(\mathbf{r},\tau)$, i.e.,

$$\left(\nabla^2 + K^2(\tau)\right) G_1(\mathbf{r},\tau) = -S(\mathbf{r})/D\,, \tag{21.19a}$$

$$K^2(\tau) = (-v/D)\left(\mu_a + \alpha k_o^2 \mu_s' \left\langle \Delta\mathbf{r}^2(\tau)\right\rangle / 3\right). \tag{21.19b}$$

For an infinite homogenous medium with a point source at the origin, this equation will also have the well known spherical-wave solution, i.e., $\sim[\exp\{-K(\tau)\mathbf{r}\}/D4\pi\mathbf{r}]$.

The mean-square displacement $\langle \Delta\mathbf{r}^2(\tau)\rangle = 6D_B\tau$ for organelles or cells undergoing Brownian motion with "particle" diffusion coefficient D_B. For the important case of random flow that can arise in the tissue vasculature, $\langle \Delta\mathbf{r}^2(\tau)\rangle = \langle V^2\rangle\tau^2$, where $\langle V^2\rangle$ is the second moment of the cell speed distribution. In the latter case the correlation function will decay exponentially as τ.

Multidistance measurements of $G_1(\mathbf{r},\tau)$ provide dynamical information about the motions within the sample in exactly the same way that diffusive waves provide information about scattering and absorption properties. The layout of the sources and detectors is similar to the diffusive wave schemes, but the correlation measurements are a little more complex. For the measurements, one needs a special piece of equipment called an autocorrelator, which takes the detector output and uses the photon arrival times to compute $G_1(\mathbf{r},\tau)$ or (more precisely) its light *intensity* analog.

The entire set of formalisms for imaging outlined in Sections 21.2.5.2 and 21.2.5.3 is applicable to diffuse light temporal correlations. The technique is attractive because it enables us to measure the blood flow (i.e., $\langle \Delta \mathbf{r}^2(\tau) \rangle$) within deep tissues. The ability to measure relative changes concurrently in blood flow, hemoglobin concentration, and hemoglobin oxygenation within a single instrument makes possible a range of cerebral studies in animal models and in infants and neonates (see References 159 through 161).

21.2.7 Contrast Agents

The use of contrast agents in DOT and spectroscopy for disease diagnostics and for probing tissue functionality follows established clinical imaging modalities such as magnetic resonance imaging (MRI),[162–164] ultrasound,[164–166] and x-ray computed tomography (CT).[164,167,168] Contrast agent administration provides for accurate difference images of the same heterogenous tissue volume under nearly identical experimental conditions; this approach often yields superior diagnostic information. Although contrast agents most commonly induce changes in absorption, recently fluorescent/phosphorescent agents have also been considered as means to increase specificity and sensitivity for tumor detection and imaging.[77,169–184] In addition to concentration changes, fluorophore lifetime is sensitive to physiological environment, for example, through oxygen quenching or pH. Most contrast agent schemes rely on the fact that the exogenous macromolecular structures accumulate preferentially in abnormal tissues.

21.2.7.1 Fluorescent Contrast Agents

A chapter in this handbook already reviews contrast agents in photon migration, so we will be very brief. (Our discussion follows from References 185 through 187.) Suppose a heterogeneous turbid medium with fluorophore distribution $N(\mathbf{r})$ is excited by an excitation diffusive wave, $\Phi(\mathbf{r},\mathbf{r}_s)$, emitted from $\mathbf{r}_s$ and whose optical wavelength is in the absorption band of the fluorophore. A fluorescent diffuse photon density wave, $\Phi_{fl}(\mathbf{r},\mathbf{r}_s)$, is produced in the medium, and

$$\Phi_{fl}(\mathbf{r},\mathbf{r}_s) = \int G_{fl}(\mathbf{r},\mathbf{r}')T(\mathbf{r}')\Phi(\mathbf{r}',\mathbf{r}_s)d\mathbf{r} \tag{21.20a}$$

where

$$T(\mathbf{r}') = \varepsilon \frac{\tau}{\tau_o} \frac{\eta N(r)}{1-\omega\tau} . \tag{21.20b}$$

The integration is over the sample volume. Here $T(\mathbf{r})$ is a fluorescence transfer function, which depends on the fluorophore radiative and total lifetimes, τ_o and τ respectively, the source modulation frequency ω, the fluorophore extinction coefficient ε, the fluorescence quantum yield η, and the fluorophore distribution $N(\mathbf{r})$. In principle, τ_o and τ (and even ε and η) can also depend on position. The Green's function $G_{fl}(\mathbf{r}, \mathbf{r}')$ is derived with a diffusion equation (Equation 21.8) for the fluorescent diffuse photon density wave at the emission wavelength, i.e., the absorption and scattering coefficients in this diffusion equation are defined at the fluorescent emission wavelength. Equation 21.20 is very similar to the equations we inverted in Sections 21.2.5.2 and 21.2.5.3. However, it is deceptively simple because heterogeneity information is embedded in Φ and G_{fl}, in addition to N and τ. Nevertheless, it can be inverted numerically using similar techniques.

21.2.7.2 Differential Absorption

In these measurements optical data are typically obtained before and after administration of the absorbing optical contrast agent (e.g., the intraveneous administration of ICG. In principle, DOT images taken before and after administration may be reconstructed and subtracted; however, in practice a more robust approach derives images of the differential changes due to the extrinsic perturbtion. In the latter case experimental measurements use the exact same geometry within a short time of one another, thereby minimizing positional and movement errors and instrumental drift. Furthermore, the use of differential measurements eliminates systematic errors associated with the different medium often required to calibrate operational parameters of the instrument or to provide a baseline measurement for independent reconstructions. Finally, the effect of surface absorbers such as hair- or skin-color variation is also minimized.

The main analytical difficulties of the differential approach arise because the media are inhomogeneous. Thus the total diffuse light field in the contrast agent perturbation problem does not separate into a homogeneous background field and a scattered field in a straightforward way. Furthermore, the average background optical properties, particularly the absorption, can change as a result of contrast agent administration.

In the typical experiment, relative absorption changes are much larger than scattering changes and one can ignore the relative changes in scattering. Under these circumstances the differential signal $\Delta\Phi$, can be related to the differential absorption $\Delta\mu_a$ via the integral relation:[188]

$$\Delta\Phi(\mathbf{r},\mathbf{r}_s) = \int W_a'(\mathbf{r},\mathbf{r}',\mathbf{r}_s)\Delta\mu_a(\mathbf{r}')d\mathbf{r} + C\,. \tag{21.21}$$

Here W_a' is a weight function very similar to the functions discussed in Section 21.2.5.2. C is a correction; it is an integral that depends on source-detector geometry and on the weight function before and after administration of the contrast agent. For many geometries (e.g., the transmission geometry) C is small and can be ignored. In those cases we can directly invert Equation 21.21 according to the ideas described in Sections 21.2.5.2 and 21.2.5.3, and thus obtain the differential absorption changes directly from difference measurements.

21.3 Instrumentation

The basic imaging geometry for diffuse optical tomography consists of a set of distinguishable point-like sources and a set of photodetectors, each covering a small area of <10 mm^2 on the surface of the medium. In general some type of source encoding strategy must be used so that the origin of the detected signals can be traced to specific sources. In this way, measurements with differing spatial sensitivities are obtained, and an image can be reconstructed.

There are three common measurement geometries: (1) planar transillumination measurements, (2) cylindrical measurements, and (3) reflectance measurements. All three are used for breast imaging (transillumination,[10–13,189] cylindrical,[15,190–192] and reflectance.[119,137,193]). The cylindrical and reflectance geometries are used for imaging animals, human baby heads,[28,194–197] and limbs on the human body (e.g., arm or leg). The reflectance geometry is used for imaging human adult heads.[159,198–200]

In Section 21.2.2 we identified three diffuse light excitation schemes: (1) illumination by subnanosecond pulses of light, (2) CW illumination, and (3) radio-frequency (RF) amplitude-modulated illumination. Short-pulse systems[201–205] detect the temporal distribution of photons as they leave the tissue. The shape of the distribution provides information about tissue optical parameters. Although these systems provide the most information per source-detector pair for characterizing optical properties, their relatively poor signal-to-noise ratio (SNR) leads to longer image acquisition times (typically a few minutes in systems used today).

CW systems[195,206–208] emit light of constant intensity or amplitude. (Sometimes the emitted intensity is amplitude modulated at frequencies less than a few tens of kilohertz.) Detectors measure the amplitude of the light transmitted through the tissue. These systems are simple to build and provide fast image rates (presently up to 100 Hz), but their lack of temporal information makes quantitation of tissue absorption and scattering more difficult. In RF systems[209–211] the light source intensity is amplitude modulated at frequencies of tens to hundreds of megahertz. Information about the absorption and scattering properties of tissue is obtained by recording amplitude decay and phase shift (delay) of the detected signal with respect to the incident wave.[211,212] These systems offer the fast image acquisition rate of CW systems and contain information sufficient for quantitative characterization of absorption and

TABLE 21.1 Comparison of Relative Advantages and Disadvantages of Time-Domain, Frequency-Domain, and Continuous-Wave Instrumentation

Instrumentation	Advantages	Disadvantages
Time-Domain	Full temporal impulse response Quantitative	Difficult to maintain Expensive optoelectronics
Frequency-Domain	Diffusive wave phase and amplitude Faster than time-domain Lower cost than time-domain	Difficult RF electronics
Continuous-Wave	Lowest cost Easy electronics Fastest Accurate for differential measurements of optical properties	Diffuse light amplitude only Less accurate for extimates of absolute optical properties

scattering optical properties. The advantages and disadvantages of the three systems are outlined in Table 21.1.

In DOT it is desirable to make a large number of measurements for image reconstruction in a short period of time so that the data are not confounded by physiological or movement artifacts. The balance between number of measurements and image acquisition time is dictated by application. CW systems are popular for imaging spatial variations of absorption changes on timescales of seconds to minutes, for example, imaging muscle[213,214] and brain activation.[195,196,198] CW systems usually have the best SNR and lend themselves well to several encoding strategies enabling massively parallel measurements. Furthermore, although CW systems are poor at quantifying static absorption and scattering properties uniquely, they excel at quantifying spectroscopic changes in absorption and scattering, particularly when *a priori* knowledge of the spectroscopic features is available. On the other hand, RF and time-domain systems are popular for imaging static optical properties when quantitative accuracy is required and when data acquisition times of one to several minutes are acceptable.

21.3.1 Source Encoding Strategies

If cost is not an issue, then increasing the number of parallel detectors or detection systems is a straightforward approach to increasing the number of measurements per unit time. Often, however, measurements with multiple source wavelengths and source positions are desired. In this case an encoding strategy enabling the separation of source wavelengths and positions must be employed. The encoding strategies currently used in CW systems and applicable to RF systems are switched-source time-division multiplexing (SS-TDM), phase-division multiplexing (PDM), pulse-modulated time-division multiplexing (PM-TDM), frequency-division multiplexing (FDM), and wavelength-division multiplexing (WDM). SS-TDM and WDM are applicable to time-domain imaging systems as well.

For SS-TDM, sources are modulated at the same frequency and cycled through consecutively; the detectors synchronously obtain the source signal through their own demodulators. This is the easiest system to design and build. Because at any given time only a single source illuminates the sample, interchannel crosstalk is low, and simple circuit construction techniques (point-to-point wiring, Protoboards, etc.) can be used successfully.

For PDM, two sources are modulated with a square-wave at the same frequency, but in phase quadrature (i.e., at a 90° phase difference). Each of the detectors synchronously detects each source through two separate demodulators and low-pass filters, each of which is "tuned" to the in-phase source. Source pairs can then be cycled through consecutively. This is an easy system to design and build, but component layout affects performance, particularly interchannel crosstalk.

For PM-TDM, M sources are cycled on and off in sequence, but at a rapid (~kHz) rate. For *N* detectors, each source is synchronously detected through individual demodulators, each of which is time-gated to one source. This approach has all the benefits of SS-TDM, but with no temporal skew. The system can be difficult to design and construct due to the complex interdigitation and fast switching speeds. Because only one source operates at any one time, the background level is very low.

For FDM, each of the sources is modulated at one of a number of anharmonically related frequencies (to minimize the effects of intermodulation distortion). For each of the detectors, the sources are demodulated coherently (synchronous detection) or incoherently (envelope detection). This is the most complex system to design and build due to the high potential for interchannel crosstalk. The high background flux arising because all sources are on simultaneously raises the shot noise floor and can saturate photo-detectors. However, because each source is "on" all the time, the scheme is more parallel than the sequential approaches described previously.

WDM simply uses bandpass optical filters in front of the photodetectors to distinguish different wavelength sources. This method can be used in combination with any of the encoding strategies described earier to distinguish light from different spatial locations.

21.3.1.1 Continuous-Wave Imaging System

As an example of the CW imaging system, we consider one used at the Massachusetts General Hospital-Nuclear Magnetic Resonance (MGH-NMR) Center. This system employs the FDM scheme to detect 32 lasers with 32 detectors (see Figure 21.5). At present, the 32 lasers are divided into 16 lasers at 690 nm and 16 at 830 nm. These 16 laser pairs are fiber coupled and deliver light to 16 positions on the medium to be imaged. The detectors are avalanche photodiodes (APDs, Hamamatsu C5460-01). A master clock generates the 32 distinct frequencies between 6.4 and 12.6 kHz in approximately 200-Hz steps. These frequencies are then used to drive the individual lasers with current stabilized square-wave modulation. Following each APD module is a bandpass filter, cut-on frequency of ~500 Hz to reduce 1/f noise and the 60-Hz room light signal, and a cut-off frequency of ~16 kHz to reduce the third harmonics of the square-wave signals. After the bandpass filter is a programmable gain stage to match the signal levels with the acquisition level on the analog-to-digital converter within the computer. Each detector is digitized at ~45 kHz and the individual source signals are then obtained by use of a digital bandpass filter — for example, a discrete Fourier transform or an infinite-impulse-response filter.

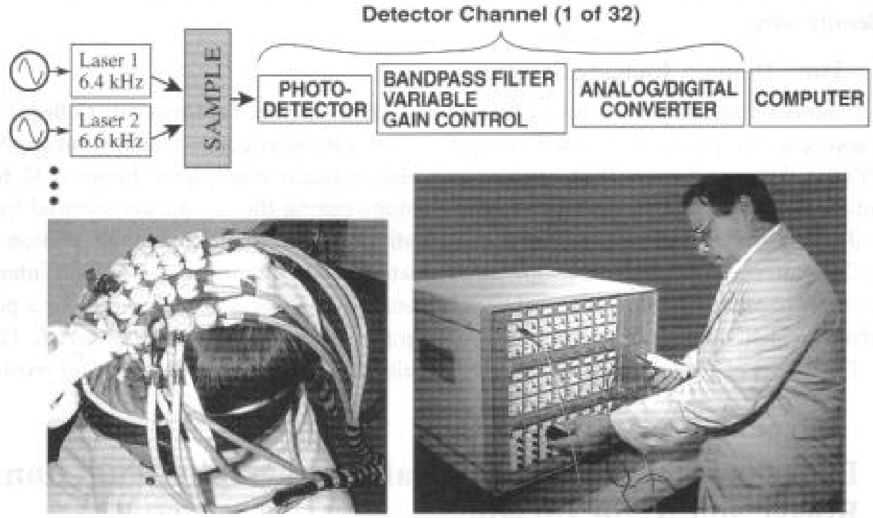

FIGURE 21.5 The MGH-NMR Center CW imaging system with 32 lasers and 32 detectors along with a block diagram indicating the frequency encoded sources and electronic processing steps from the photodetector to the computer memory.

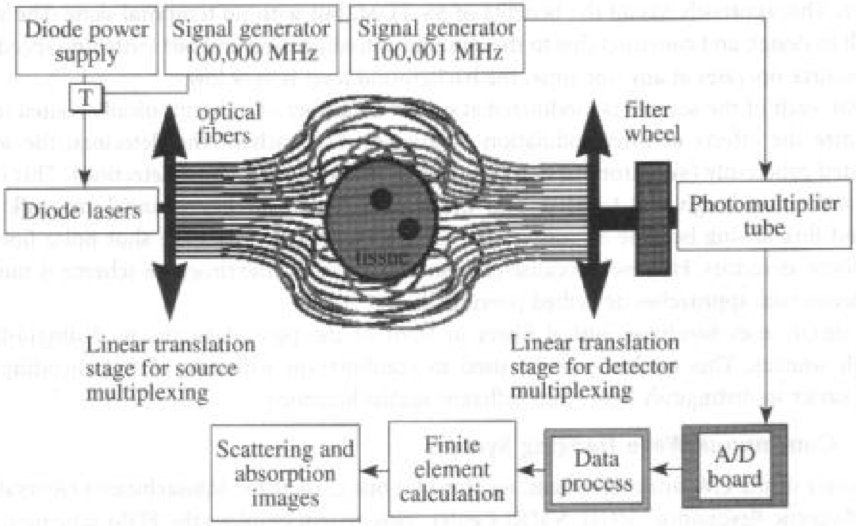

FIGURE 21.6 Schematic of the frequency-domain imaging system developed at Dartmouth College. (From Pogue, B.W. et al., *Opt. Express*, 1, 391, 1997. With permission.)

21.3.1.2 Frequency-Domain Imaging System

A typical frequency-domain imaging system is illustrated in Figure 21.6. Developed at Dartmouth College,[215] this system modulates the intensity of a laser diode at 100.000 MHz and couples the light sequentially into different fiber optics (the SS-TDM encoding scheme). Diffusely remitted light is captured by detector fibers that are coupled into a single photomultiplier tube (PMT). The PMT is time-shared between the individual detector fibers, so the instrument employs a TDM encoding scheme. A filter wheel is positioned before the PMT to prevent saturation of the detector by stronger optical signals coming from closer to the source. The photo-electric signal within the PMT is modulated at 100.001 MHz to heterodyne the signal down to 1 kHz. The 1-kHz signal is acquired by an analog-to-digital converter, from which a computer calculates the relative amplitude and phase of the detected 100-MHz diffuse photon density wave.

21.3.1.3 Time-Domain Imaging System

Figure 21.7 shows a diagram of the time-domain image system developed at University College London.[216] The light source is a subpicosecond pulsed Ti:Sapphire laser with wavelength tunable from approximately 750 to 850 nm. Laser pulses are fiber coupled and fiber-optically multiplexed between 32 fibers that deliver source light to 32 independent positions. Photons exiting the sample are received by 32 large diameter detector fibers that relay the light to 32 individual time-correlated single photon counting channels. Computer controlled variable optical attenuators ensure that the detected light intensity does not saturate the photodetectors. The arrival time of detected photons is histogrammed by a picosecond time analyzer, which simultaneously produces histograms of the measured TPSF for all 32 detector channels. The full set of TPSFs for all source-detector pairs represents the raw data used for reconstructing images.

21.4 Experimental Diffuse Optical Tomography: Functional Breast and Brain Imaging

The imaging systems described previously and others like them have been used in phantom, animal, and human subject studies. In this section we provide a coherent snapshot of these activities. We begin with

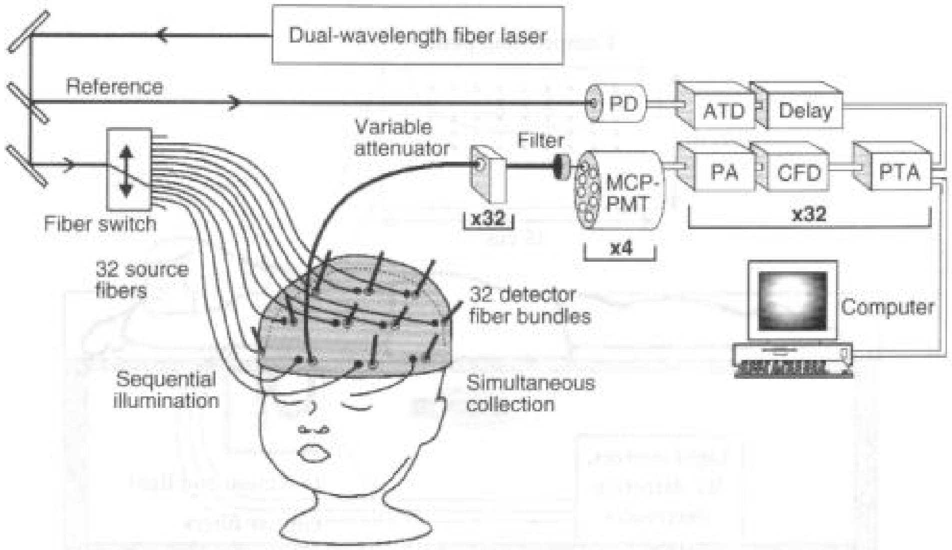

FIGURE 21.7 Schematic diagram of the time-domain imaging system. For clarity, only one detector fiber bundle is shown. PD = photo diode; PA = pre-amplifier; ATD = amplitude timing discriminator; CFD = constant fraction discriminator; PTA = picosecond time analyzer.

a tissue phantom experiment in order to illustrate image reconstruction on a controlled sample; the DOT reconstructions produce acceptable images by striking a balance between image noise, contrast, and resolution. Next we review the application to breast imaging, with recent clinical results. We describe measurements of normal breast optical properties, of tumors based on endogenous contrast, and of tumors using exogenous contrast agents to enhance tumor absorption characteristics preferentially.

Finally, we review the application to functional brain imaging. In this case we show images of blood flow, blood volume, and oxygen saturation changes in a rat stroke model. Then we show images that reveal localized variations in cerebral hemodynamics due to a sensory stimulation of a rat. Finally, we provide an example of functional brain imaging in adult humans with motor-sensory stimuli. The experiments presented are not exhaustive and do not represent the full range of results from the community. Nevertheless, the selected experiments indicate the promise of DOT for *in vivo* functional imaging.

21.4.1 Multiple Absorbers in a Slab Phantom

In this subsection we show how DOT is able to resolve multiple perturbations in the optical properties of a highly scattering medium. We also illustrate the trade-off between image resolution and the contrast-to-noise ratio. This type of experiment is important because it validates DOT techniques in well controlled samples.

The experimental data were collected using a hybrid CW and RF system developed at the University of Pennsylvania[217,218] (see Figure 21.8). Laser light is multiplexed to 45 positions (a 9 × 5 array) on one side of the slab phantom (i.e., parallel planes, see Figure 21.8). Nine detector fibers are interspersed within the 9 × 5 array to receive a 70 MHz frequency-domain signal, simultaneously, from which the amplitude and phase is determined by an IQ-homodyne demodulation.[219] This frequency-domain information was used to determine the background optical properties of the medium. A 16-bit CCD camera (Roper Scientific, NTE1340) was positioned to image the CW light transmitted through the phantom. The CCD camera had 800 × 1120 pixels, which were binned 24 × 24. The measurements were cropped to within a radius of 6 cm of the maximum transmitted signal producing approximately 250 independent measurements (i.e., a 21 × 13 detector array) per source position.

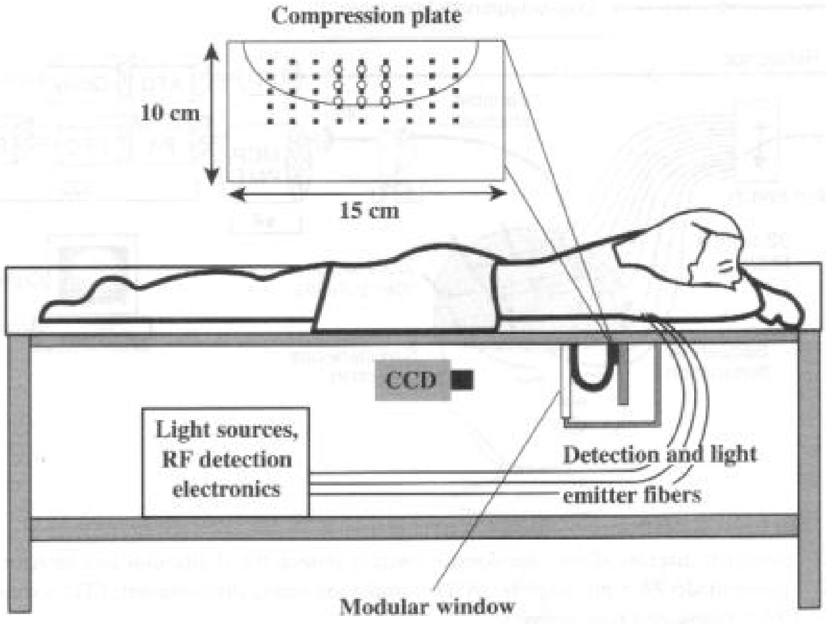

FIGURE 21.8 Phantom geometry for the transillumination measurements. The array of 9 × 5 light sources is indicated in the compression plate by the black squares. The 3 × 3 array of frequency-domain photodetectors intermingled with the source fibers is indicated by the open circles. A CCD camera images the transmission of the CW light from each source position individually. A slightly modified version of this experimental system was used for the clinical measurements described in Section 21.4.1, with the CCD camera replaced by a scanning frequency-domain photodetector.

For the phantom experiment, the breast tank was filled with an Intralipid/ink solution (see Figure 21.8)[220,221] with $\mu_s' = 8$ cm^{-1} and $\mu_a = 0.05$ cm^{-1}. In one experiment, two highly absorbing spheres ($\mu_a = 2$ cm^{-1} and $\mu_s' = 8$ cm^{-1}) were suspended in the Intralipid solution with a 5-cm separation; in another experiment many more spheres were suspended in the Intralipid solution. The image reconstruction algorithm was formulated using the Rytov approximation to the integral solution of the diffusion equation (see Section 21.2.5.2). A finite difference scheme was used to solve the forward problem in the rectangular geometry, and a conjugate gradient method was used to solve the inverse problem. Regularization was used for the inverse problem (see Section 21.2.5.3), and the entire scheme was iterative. Convergence was consistently obtained after 15 iterations.

An image of the two spheres was reconstructed with optimal regularization (see Figure 21.9). The three-dimensional image shows that two absorbers are easily resolved. The optimal regularization parameter was determined by examining the dependence of the regularization parameter on image norm, image variance, full-width at half-maximum (FWHM) of the imaged absorber, and measurement residual (see Figure 21.10). When the numerical value of the regularization parameter was increased, the image norm and image variance decreased, but at the expense of decreased image resolution (i.e., an increase in FWHM of the spheres) and increased measurement residual. A plot of the image contrast-to-noise ratio vs. the regularization parameter indicates that contrast-to-noise ratio is optimized with a regularization parameter that balances image noise and resolution (see arrows in Figure 21.10).[217] Similar trade-offs between image noise and resolution can be expected when imaging animals and human subjects. Culver et al.[217] also demonstrated images of many (i.e., >10) spheres in the same sample volume, thus indicating the potential of DOT for reconstructing multiple heterogeneities (as opposed to isolated heterogeneities in a homogenous background).

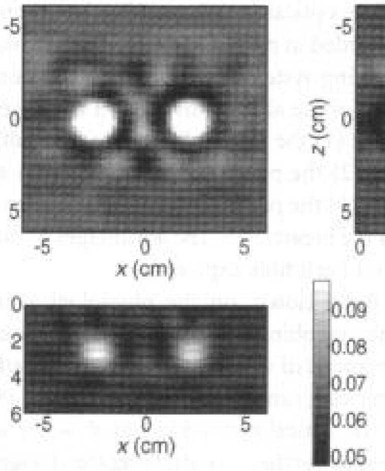

FIGURE 21.9 Three slices of the three-dimensional absorption image reconstructed from the phantom data are shown. The *x-z* plane is parallel to the measurement planes of the phantom. The scale bar indicates the range of values for the absorption coefficient.

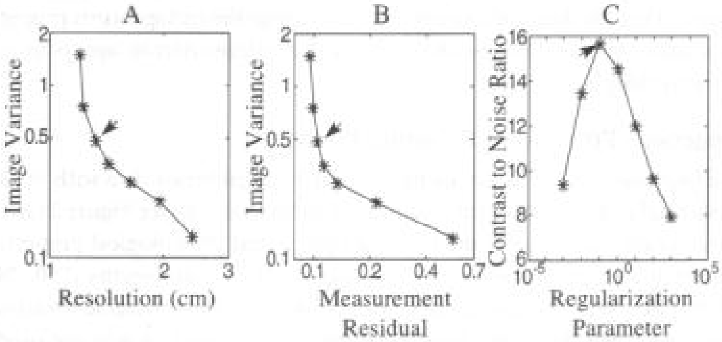

FIGURE 21.10 The dependence of objective measures of image quality on the regularization parameter is shown. (A) Increasing the regularization parameter controls the trade-off between image noise and resolution. (B) Increasing the regularization parameter also increases the residual of the fit to the experimental data. (C) The optimal regularization parameter as determined by the maximum image contrast to noise ratio corresponds to the points in (A) and (B) that balance image noise and resolution/measurement residual (indicated by the arrows in each figure).

21.4.2 Breast Imaging

The use of light to detect tumors in the breast was first proposed by Cutler in 1929,[83] who hoped to be able to distinguish between solid tumors and cysts in the breast by illuminating the breast and shadowing the tumors. However, he found it difficult to produce the necessary light intensity without exposing the patient's skin to extreme heat, while the low resolution of the technique severely limited its clinical applications. With the advent of more modern optical sources and detectors, optical transillumination breast imaging was tried again in the 1970s and 1980s, but was abandoned because of lack of sensitivity and specificity.[93,222,223] The burst of activity in the 1990s can be traced to widespread acceptance of the diffusion approximation, which provides a tractable basis for tomographic approaches to image reconstruction using highly scattered light. Tomographic methods are crucial for recovery of information about heterogeneous breast tissues.

Functional, tomography-based diffuse optical breast imaging has been demonstrated, but further understanding and improvements are needed in order for it to become clinically useful. Current research is focusing on the construction of imaging systems with higher resolution and increased quantitative accuracy, as well as on the improvement of the algorithms used in image reconstruction. Thus far three general patient positions have been used: (1) the patient lies prone on a cot with a breast (or breasts) in a pendant position for imaging;[15,190–192] (2) the patient sits or stands with a breast held in compression similar to x-ray mammography;[10–13] and (3) the patient lies supine and is imaged with a hand-held probe that is moved to different positions on the breast.[119,193] The advantages of one approach over another for extraction of optical properties have not been fully explored.

Current research is also focusing more closely on the physiological information available to the technique. For example, quantitative hemoglobin images of the female breast showed localized increases in hemoglobin concentration that corresponded with biopsy-confirmed pathological abnormalities, suggesting that NIRS is capable of characterizing tumors as small as 0.8 ± 0.1 cm.[15] Other investigators have focused on the intrinsic sensitivity of the optical method to blood, water, and adipose — the principal components of the breast. Many of these researchers are studying the changes in breast optical properties associated with age, exogenous hormone levels, and menopausal status as well as, to a lesser extent, fluctuations in menstrual cycles.[14,224] Still other researchers are exploring the use of contrast agents[13,225,226] and the combination of DOT with other imaging techniques such as MRI and ultrasound.

In this section we briefly review some recent advances in the application of DOT to breast imaging. Our first example establishes the baseline optical properties of the normal breast; such information provides a useful benchmark about the requirements for detection of tumors based on endogenous (and exogenous) contrast. Then we describe experiments that image the endogeneous properties of the breast, revealing tumor signals, and we describe experiments that utilize contrast agents to create images with improved tumor sensitivity.

21.4.2.1 Endogenous Properties of Normal Breast

Our group at the University of Pennsylvania has collected optical breast data with the subject in a prone position, using essentially the same system discussed in Reference 218 (see Figure 21.8). The goal of these measurements was to establish *in-vivo* the baseline optical and physiological properties of the normal breast. The experimental system employed diode lasers at three wavelengths (750, 786, and 830 nm), each modulated at 140 MHz. The source light was delivered to the moveable breast-stabilization plate through an optical fiber. For detection, the CCD camera in Figure 21.8 was not used; instead a fiber-coupled PMT was scanned to multiple positions on the breast with the source fiber fixed at the center of the tissue and scan region. Prior to collecting data, the tank surrounding the breast is filled with a scattering liquid whose optical properties closely approximated the breast tissue. The amplitude and phase of the transmitted DPDW was measured using a homodyne IQ demodulation scheme.[219] In 15 min, 153 measurements (17 × 9) are obtained over an area of 10 cm × 7 cm (x,y).

Measurements were collected on 52 healthy volunteers. The analysis had one new innovative feature: the data were fit simultaneously at all three wavelengths and "reconstructed" using spectral responses of oxy- and deoxyhemoglobin, and a Mie-based model for the wavelength dependence of the scattering coefficient. This spectroscopically self-consistent approach reduced crosstalk between scattering and absorption, overcoming some of the limitations of the homogeneous tissue model often used for characterization. The average absorption and scattering coefficients of the normal breast tissue were found to be $0.041 \pm 0.025\ \text{cm}^{-1}$ and $8.5 \pm 2.1\ \text{cm}^{-1}$, respectively, at 786 nm. The mean blood volume and blood oxygen saturation were found to be $34 \pm 9\ \mu M$ and $68 \pm 8\%$, respectively.

A scatter plot of the blood volume and blood saturation results is shown in Figure 21.11. We see from this plot that the optical method will be sensitive to tumors with large blood volume and low blood saturation (outside the dashed lines); this condition might prevail in many tumors. A weak correlation of total hemoglobin concentration and scattering with body mass index (BMI) was found (i.e., decreasing with increasing BMI), but no statistically significant correlation with age was observed (20 to 65 years). This information provides insight into the types of intrinsic contrast available to optical breast imaging